Article

Flexible electronic-photonic 3D integration from ultrathin polymer chiplets

Check for updates

Yunxiang Huang[1,3], Gen Li[1,3], Tianyu Bai [1], Yieljae Shin [1], Xiaoxin Wang[1], Alexander Ian More[2], Pierre Boucher[2], Chandramouli Chandrasekaran [2], Jifeng Liu[1] & Hui Fang [1] ✉

Integrating flexible electronics and photonics can create revolutionary technologies, but combining these components on a single polymer device has been difficult, particularly for high-volume manufacturing. Here, we present a robust chiplet-level heterogeneous integration of polymer-based circuits (CHIP), where ultrathin polymer electronic and optoelectronic chiplets are vertically bonded at room temperature and shaped into application-specific forms with monolithic Input/Output (I/O). This process was used to develop a flexible 3D integrated optrode with high-density microelectrodes for electrical recording, micro light-emitting diodes (μLEDs) for optogenetic stimulation, temperature sensors for bio-safe operations, and shielding designs to prevent optoelectronic artifacts. CHIP enables simple, high-yield, and scalable 3D integration, double-sided area utilization, and miniaturization of connection I/O. Systematic characterization demonstrated the scheme's success and also identified frequency-dependent origins of optoelectronic artifacts. We envision CHIP being applied to numerous polymer-based devices for a wide range of applications.

Integrated electronic-photonic systems have a wide range of applications, such as optical wireless communications[1,2] and biosensing[3,4]. In polymer-based, flexible systems, integrated electronic-photonic devices have emerged as strong contenders for optogenetic neurostimulation[5–8], photo-plethysmography sensing[9–11], and continuous glucose monitoring[12,13] due to their biocompatibility and tissue-conforming ability[14–16]. Given that for many applications, there are space constraints, the interfacing devices typically cannot be made from standard printed circuit board (PCB) manufacturing[17,18,19]. Moreover, integrated electronic-photonic devices require combining various electronic and photonic components such as electrodes, sensors, and light sources, each of which relies on separate fabrication, necessitating complex manufacturing. As an example, integrating these components into a single chip within semiconductor manufacturing is conventionally achieved in a cumbersome sequential fabrication process with different metallization layers[8,14,20,21] and also using specialized silicon wafers[22] or through epilayer transfer of III-V photonic materials[23], which can lead to low yield and high cost. To address the mismatch between Si and III-V semiconductors, tremendous efforts have established micro-transfer printing of fully formed device elements[7,24] as a practical way of integrating photonic components. This establishment is especially true for flexible integrated systems, where epitaxy cannot be performed on polymer substrates. Building on this success, micro-scale stacking has enabled the integration of different flexible device layers, though generally after the device micro-profile definition[7,25–29]. As a result, it is challenging to achieve

device miniaturization or volume production. Overcoming these challenges would enable advanced device capabilities such as minimally invasiveness in medical diagnostics and therapies, as well as cost-effective device manufacturing for affordable and equitable technology accessibility.

Here, we report a robust, scalable 3D-integration scheme - chiplet-level heterogeneous integration of polymer-based circuits (CHIP) - for fabricating advanced, flexible electronic-photonic integrated devices. This scheme first leverages co-design and parallel fabrication of polymeric chiplet layers with different device functions. After the chiplet fabrication, vertically aligning and bonding of post-fabricated chiplet layers using ultrathin biocompatible adhesives at room temperature achieve 3D function integration with monolithic I/Os. To illustrate this process, we demonstrated a proof-of-concept 3D-integrated optrode system with high-density arrays of μLEDs and microelectrodes. Using CHIP, for the first time, we achieved (i) chiplet-level 3D integration of all needed functions, including temperature sensing and optoelectronic shielding capabilities for a thermal safe, low noise, and artifact-free bio-optrode; (ii) simplified double-sided area utilization, which would otherwise be not achievable without backside lithography and is highly challenging for Si-based devices; and (iii) miniaturization of the connection for the final 3D-integrated device. Systematic experimental studies and simulations revealed the integrated system's mechanical flexibility, high performance of electrical, optical, and thermal functions, and remarkable reliability. In addition to multifunctional incorporation, the new 3D-integrated platform also enabled device physics studies in flexible

[1]Thayer School of Engineering, Dartmouth College, Hanover, NH, USA. [2]Department of Anatomy & Neurobiology, Boston University, Boston, MA, USA. [3]These authors contributed equally: Yunxiang Huang, Gen Li. ✉e-mail: hui.fang@dartmouth.edu

electronic-photonic systems and revealed frequency-dependent origins of optoelectronic artifacts on polymeric substrates, where low-frequency-band artifacts are light-induced, and high-frequency-band ones are from electrostatic effects, a key insight useful for future device design and system integration. We envision the CHIP approach here to be widely generalizable and produce a wide variety of advanced device technology with the integration of unprecedented multifunctionalities while with a strong ability of miniaturization and excellent manufacturability.

Results

The CHIP process and prototype multifunctional device demonstration

Figure 1a illustrates the CHIP processing steps towards achieving a demonstration prototype of a 3D-integrated flexible optrode, which is typically used for neuronal recording with optogenetic stimulation. Initially, the microelectrodes, temperature sensors, and shielded μLEDs were co-designed but separately fabricated on Kapton substrates laminated on polydimethylsiloxane (PDMS)-coated glass handling substrates as polymer chiplets (#1–3). This strategy can ensure a high yield of each function using post-fabrication characterization before the CHIP bonding process. For the μLED chiplet fabrication, we leveraged transparent colorless Kapton and adopted a monolithically selective micro-transfer printing technique with metallization after the printing (Supplementary Fig. 1). An additional thin-film shielding interlayer was deposited and patterned on the backside of the μLED chiplet to prevent functional crosstalk. After the complete fabrication, the microelectrode and temperature sensor chiplets were directly peeled off from the handling substrates and were aligned and bonded onto the μLED chiplet sequentially using an room-temperature-(RT)-curing biocompatible epoxy resin. Finally, a UV-laser profiling completed the fabrication, achieving the CHIP process with a monolithic device ready to be peeled off from the handling substrate. Compared to the Si-based sequential fabrication process for double-sided functional integration[23], this CHIP processing step is easy for double-sided area utilization by simply flipping device layers and bond them, and robust for 3D heterogeneous integration without extra physical, chemical, and thermal treatments for functional assembly[7,26,27,30,31]. Besides, if there is a need to achieve same-sided optical emitting and electrophysiological recording while still having the shielding function, there are potential strategies based on the CHIP process as follows: (i) turn the LED layer over and deposit exposed shielding windows just right on the top of the LED or the bottom of the electrode layer before the layer bonding; (ii) employ a flip-chip-bonding like method to print the μLEDs, thus the LED emitting surface naturally will be toward the same side as the recording electrodes.

We implemented the chiplet functions using contemporary, flexible electronic designs (Fig. 1b). The prototype 3D-integrated flexible optrode comprised a linear array of microelectrodes (twelve poly(3,4-ethylenedioxythiophene)-poly(styrenesulfonate) (PEDOT:PSS)-based electrodes, site area: $10 \times 20 \mu m^2$), a temperature microsensor (Pt-based serpentine-resistor), and a linear array of green-emitting μLEDs (six InGaN-based μLED chips with a lateral structure, chip area: $34 \times 58 \mu m^2$) with a metal shielding interlayer (Au, thickness 100 nm) for optoelectronic shielding. The 3D-integrated flexible optrode with these three chiplets bonded from the CHIP process exhibited solid and tight bonding interfaces, as examined by cross-sectional SEM (Fig. 1b). Figure 1c shows the peeling force as a function of different adhesive thicknesses of 1–10 μm. Adhesives of more than 5-μm thick cured at RT showed forces of a similar magnitude as polyimide self-adhesion cured at a high temperature[32]. As a result, we used a 5-μm thick adhesive for the prototype optrode. Detailed specifications and fabrication processes are provided in Methods and Supplementary Fig. 2. The prototype 3D-integrated flexible optrode was constructed with a specification of ~75 μm thickness, 240 μm width, 2 mm length, and 27.5° tip angle. With this scheme, the optrode has excellent bending properties, cycling multiple times without an electrical open circuit during the bending,

as shown in Fig. 1d and Supplementary Movie 1. This feature greatly differs from fragile Si-based optrodes[5,6,22]. The stress distribution simulation confirms the optrode's robust bending ability with a maximal angle of 53°, which still results in less than 5% strain, which is typically considered as the fracture strain of gold films[33]. To better analyze the strain distribution during bending, we further studied the strain in each device layer (Supplementary Fig. 3). The neutral plane located around the interface between the LED layer and temperature sensor layer experienced zero deformation during bending. The LED layer at the top experienced a large stretching yet within the safe range (strain < 5%) when bent 53°. Besides, we also included a mechanical failure analysis (Supplementary Fig. 4) in which an extreme one-time bending was applied to the device (~108°). It was revealed that the LED located close to the base failed first while the other LED close to the tip still survived. The result is consistent with the prediction from the Finite Element Analysis (FEA) in which a significantly large strain appeared around the locations of the failed LED. The locations where the LED survived still showed a safe range of strain (<5%). What's more, we also investigated the electrode impedance before, during, and after the bending (Supplementary Fig. 5). With the shank displacement from 0.5 to 1 mm, there were no obvious changes from the twelve electrodes on the shank before, during, and after the bending. On the other hand, the current CHIP-based optrode also inherits an instant insertion capability without an assisted stiff probe guide on a brain phantom[34], as shown in Supplementary Figs. 6, 7 and Movie 2.

Another important feature of the CHIP process is that during this process, the I/O connections of all functional chiplets were located next to each other facing the same side, forming one monolithic I/O pad area by design. With the monolithic I/O design, the 3D-integrated optrode can be conveniently and rapidly mounted onto a PCB connector to achieve terminal control (Supplementary Fig. 8). Compared to other approaches such as using anisotropic conductive film (ACF), this non-permanent assembly method demonstrates robust contact pressure, efficient space utilization, and a cost-saving strategy in a replaceable and labor-effective manner. In addition to miniaturization, this multifunctional integration system from the CHIP process also demonstrated high reliability of the electrical recording, temperature sensing, optical emitting, and shielding capabilities while soaked in PBS solution at 47 °C for seven weeks, as shown in Fig. 1e–h. We also investigated the electrical, optical, and mechanical functions after cycled bending (Supplementary Fig. 9). It showed no obvious difference in their impedance and light emitting from 0 to 1000 time-cycled bending. Meanwhile, the SEM images still displayed a solid structure for the tip, neck, and base of the shank sidewall after a 1000-time cycled bending test.

Compared to state-of-the-art, Si-based electronic-photonic integrated optrodes (Supplementary Table 1), all of which were achieved from sequential fabrication, the CHIP process enables unprecedented multi-function incorporation yet with much-reduced manufacturing complexity and risk from the inherent parallelism in the new process flow. Compared to previous polymer-based devices from micro-scale stacking, CHIP allows easier processing from the chiplet-level operations without the risk of contaminating exposed sensors by over-flow adhesive from micro-scale shank on both sides during the pressure and bonding, which often demands larger width or area of the optrode for reliable bonding[7]. Handling plasma-treated or magnetic thin-film substrate in liquid environments to avoid such a problem is an alternative[25,29]. However, CHIP easily avoids common challenges in processing multiple functional shank stacking as well as the potential delamination or magnetic resonance interference after implantation. With the final-step laser profiling, CHIP can achieve highly miniaturized devices that are only limited by the sub-20-μm laser spot size, which is also continuously improving. On the other hand, chiplet-level processing can enable the mass production of many devices in parallel on the same 3D-integrated device. Leveraging existing wafer-level μLED transfer-printing techniques[35], this manufacturability from CHIP holds immense potential in further scaling up toward wafer-level heterogeneous integration of polymer-based circuits (WHIP) for consumer-grade and low-cost products.
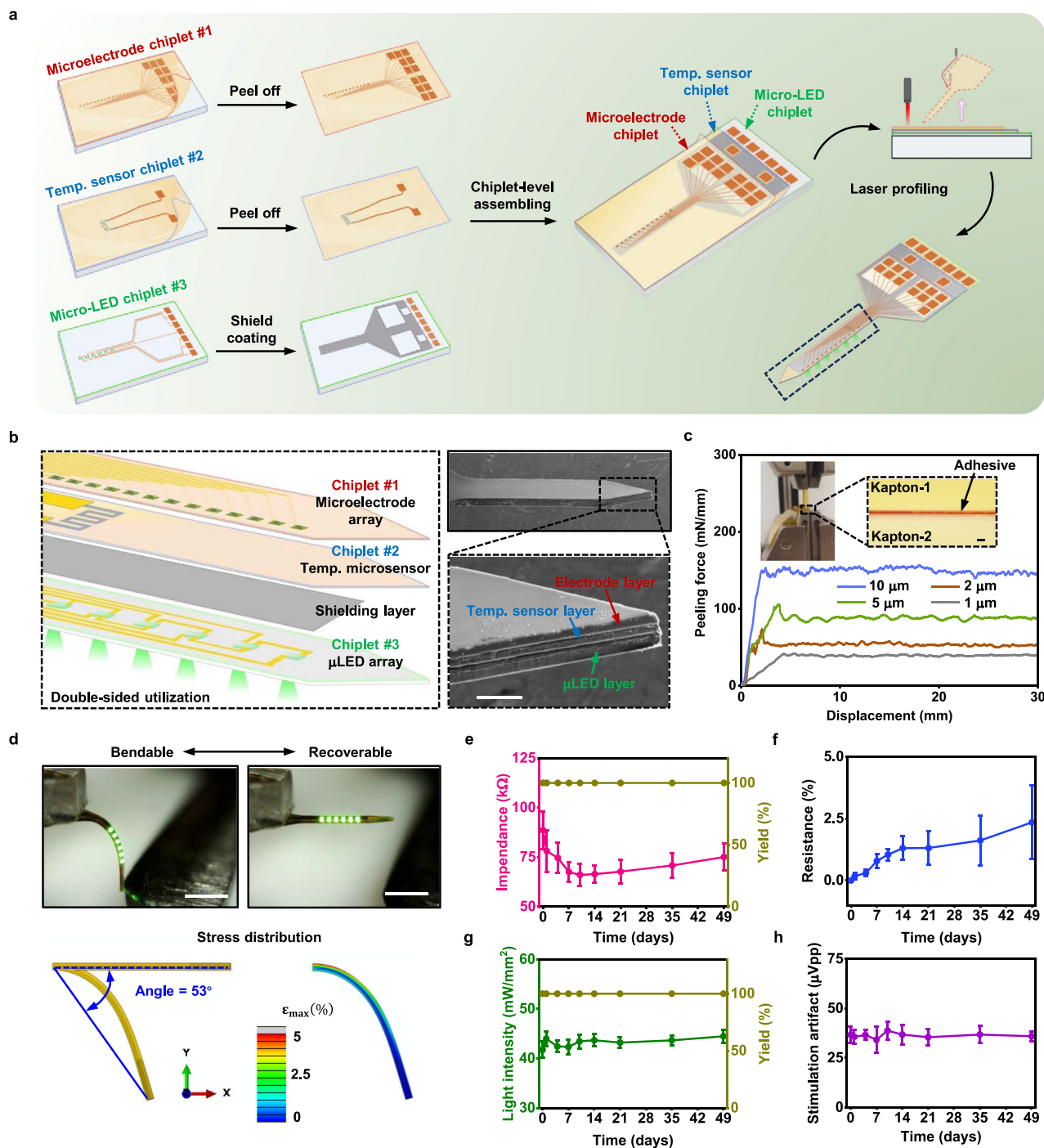
Fig. 1 | Schematic illustration of the CHIP process and its demonstration in 3D-integrated flexible optrode. a Schematic illustration of the chiplet-level integration and device profiling approach, exemplified via manufacturing a 3D-integrated flexible optrode. **b** Left: The heterogeneously integrated multifunctionality includes electrophysiological recording (twelve microelectrodes, $10 \times 20 \ \mu m^2$), temperature sensing (serpentine-shaped μ-resistor overlaying one μLED), optoelectronic shielding, and optical stimulating (6 μLEDs, $34 \times 58 \times 7 \ \mu m^3$). Right: The SEM images of the 3D-integrated shank (scale bar: 50 μm). **c** T-peeling test of the peeling force between two Kapton substrates with different adhesive thicknesses. The inset shows the measurement setup and the image of a test sample (scale bar: 1 μm). **d** Bendability and recoverability of the 3D-integrated flexible optrode (scale bar: 800 μm) and the simulation of its stress distribution during bending. **e** Measured impedance and microelectrode yield in the 3D-integrated optrode during the soak test. **f** Normalized resistance change of the temperature microsensor (20 nm thickness) during the soak test. **g** Measured light power and μLED yield in the 3D-integrated optrode during the soak test (input current 0.6 mA). **h** The recorded high-pass filtered peak-to-peak magnitudes of the stimulation artifact when all μLEDs were on in the 3D-integrated optrode (input current 1 mA). All soak tests were conducted in PBS solution at 47 °C for 7 weeks. All soak test data are presented as mean ± standard deviation of the mean (s.d.m.) ($n = 6$).

Characterizations of individual functions of the multifunctional device from CHIP

To evaluate the functionalities of the 3D-integrated flexible optrode from CHIP, we investigated its electrical recording, optical emitting, and thermal sensing capabilities through systematic experiments and simulations. Figure 2a illustrates the histogram of the impedances from the microelectrodes. These PEDOT:PSS-based electrodes possess a uniform green color with around 70–85 kΩ impedance (1 kHz) and are suitable for
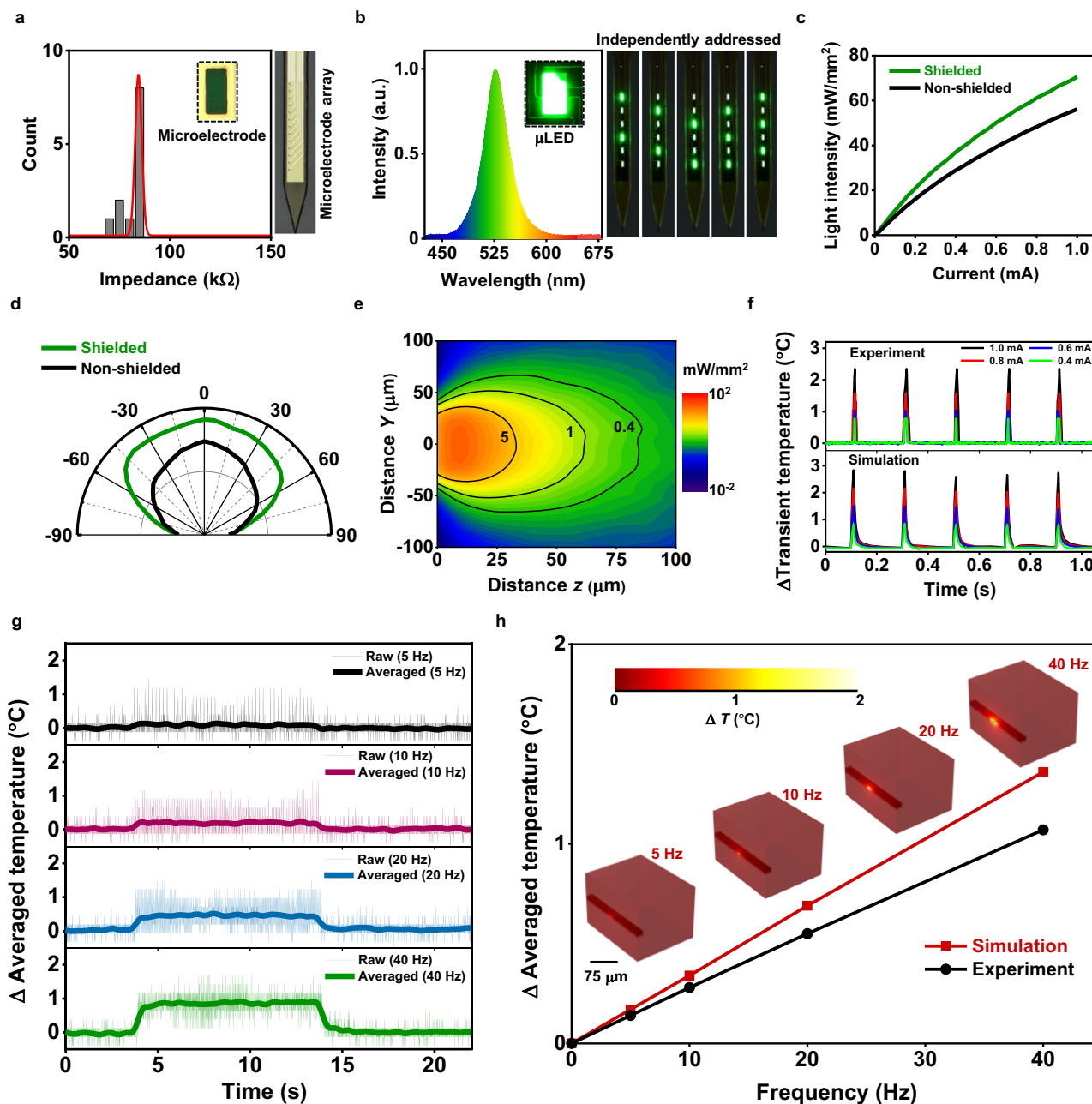
Fig. 2 | Electrical, optical, and thermal characterization of the 3D-integrated flexible optrode from CHIP. a The histogram of the electrode impedances in the microelectrode array in the integrated optrode. Inset and Right: the images of the single electrode and the array, respectively. **b** The measured wavelength spectrum of the µLED in the integrated optrode and the demonstrations of the independently addressable µLED array. **c** The measured surface light intensity of the µLED as a function of input current from both the non-shielded and shielded optrodes. **d** The measured light distribution of the µLED from both the non-shielded and shielded optrodes. **e** Simulated optical propagation of the µLED (40 mW/mm² as an initial value). **f** Measured and simulated transient temperature rise as a function of input current (pulse duration 10 ms, frequency 5 Hz). **g** Temperature rises as a function of the frequency (pulse duration 10 ms, current 0.6 mA, total time 10 s). **h** Measured and simulated averaged temperature rise as a function of frequency (pulse duration 10 ms, current 0.6 mA). The simulated thermal effects correspond to the temperature distribution around the µLED with different stimulation frequencies. All the data of the measured temperature rise was obtained using an integrated temperature microsensor. All the optical and thermal simulation data were computed based on the brain tissue environment.

recording bio-electric activities[36,37], implying that the CHIP process at RT has a potential advantage for integrating heat-sensitive materials such as PEDOT:PSS which suffers a non-recoverable electrical property degradation from thermal processing[38,39]. More information about the properties of these uniform PEDOT:PSS-based electrodes can be found in a recent study[40]. The µLED of the optrode shows a standard 525-nm emission peak wavelength under the current injection (Fig. 2b), matching many opsins' optical absorption[41]. We also created independently addressed systems for the optical array with many µLEDs (Supplementary

Movie. 3), enabling arbitrary optical stimulation combinations across different depths in the future. The shielding coating further strengthened the output optical power (Fig. 2c), presumably due to increased optical reflection from the backside metal shielding layer[42]. At an injection current of 1 mA, the individual green µLED achieved an irradiance of ~70 mW/mm², sufficiently meeting the activation threshold of 1 mW/mm² for optogenetic modulation[43,44]. This light emission is contributed by the transparent colorless Kapton substrate rather than the brown-colored one used for µLED heterogeneous integration. Besides, we also included

the light emission within the agarose gel environment (0.6%) (Supplementary Fig. 10). There were no significant differences when light penetrated through the same thick glass and agarose gel. Both non-shielded and shielded optrodes can maintain nearly Lambertian emission distributions (Fig. 2d). To illustrate the optrodes' optical resolution, we established an optical propagation model in the brain tissue. Theoretical calculations indicate that light intensities from the optrode decrease to 5–30% of the original values over a propagating distance of 50 to 150 μm (Supplementary Fig. 11). We also analyzed the excitation spatial coverage of the optrode for different currents (Supplementary Fig. 12) in which the effective simulation volume was estimated based on an intensity threshold value of 1 mW/mm^2 [45–47]. The simulated optical propagation, following a Lambertian profile, validates the theoretical calculations (Fig. 2e). On the other hand, we also predicted the light propagation when there was a gap between the μLED and targeted neurons (Supplementary Fig. 13).

To mitigate potential bio-safety issues and unwanted biological responses caused by overheating, a temperature microsensor (Pt serpentine resistor, averaged sensitivity 0.00171/°C, Supplementary Fig. 14) was incorporated, overlaying the μLED close to the optrode base, with potentially the strongest heating effect. This location was chosen based on the smaller thermal capacitance in the shallower tissue environment. Figure 2f presents the measured and simulated transient temperature rises with different μLED injection currents. The results of the simulation are similar to the experimental findings. These results showed similar rises from 1 to 3 °C within a few milliseconds as the input current increases from 0.4 to 1 mA. The response time was faster than 4 ms, limited by the 250 Hz sampling rate (Supplementary Fig. 15). This rapid response suggests the feasibility of monitoring μLED temperature dynamics using the integrated temperature sensor. Investigations into the average temperature rise with varying stimulation frequencies (Fig. 2g, h) and duration times (Supplementary Fig. 16) indicated that the maximal average temperature rise remains below 1.5 °C, even with a maximal pulsed current injection of 0.6 mA (offering ~50 mW/mm^2 light power) under conditions of 40 Hz frequency and 50 ms duration time. Normally, temperature increases of a few degrees in vivo are considered acceptable[7,8,48]. On the other hand, the optical intensity range of 1–10 mW/mm^2 is considered sufficient for optogenetic modulation[49–51]. The steady-state heat transfer simulations including 6 μLEDs configured as the real device were established to investigate the thermal effect in the extreme scenario in which all of them are turned on simultaneously (Supplementary Fig. 17). It was revealed that the multiple temperature rise peaks were aligned with the location of each μLEDs. The maximum discrepancy in temperature peak between μLEDs (center to edge) is around 0.3 °C (frequency 40 Hz, duration 20 ms, current 0.6 mA). It should be emphasized that this is also an extreme stimulation condition. For a general 10 Hz, 10-ms duration protocol, the maximum temperature discrepancy between μLEDs is around 0.04 °C.

Thus, the 3D-integrated flexible optrode from CHIP offers high-density, individually addressable optical stimulation capabilities with sufficient light power and the ability to monitor the temperature rise in real-time for bio-safety. While the material choice, optrode design, and device footprint are all with in vivo applications in mind, future studies should conduct rigorous biocompatibility evaluations according to ISO 10993–1 for translation of this technology.

Optoelectronic artifacts in polymer-based electronic-photonic integrated devices

Effectively minimizing optoelectronic artifacts to ensure high-fidelity bio-signal acquisition poses a challenge for all bio-integrated electronic-photonic systems. Different from previous Si-based integrated optrodes, polymer-based devices consisting of ultra-thin transparent polymeric encapsulation/substrate layers are exempted from the substrate photovoltaic effect[6,52]. However, the densely distributed metal interconnections of the active and passive device components from different layers inherently introduce the possibility of electrical-induced artifacts, such as inductive-induced artifacts associated with electromagnetic interference (EMI)[6,53] and capacitive-induced artifacts associated with electrostatic effects[54]. In

addition, light can also lead to photoelectrochemical effects[45,55] when active photons radiate to the electrode surface or hetero-junction interface from scattering. To mitigate the above stimulation artifacts, an effective strategy involves optoelectronic shielding between the μLED and electrode layers[6,25,28,56]. Such a shielding design was easily implemented using CHIP process. Here, we investigated the overall stimulation artifact of the 3D-integrated flexible optrode from CHIP with and without the shielding layer in Fig. 3.

Figure 3a displays the backside of the non-shielded optrode with illumination of all μLEDs, revealing densely packed parallel wires of the top μLEDs and bottom microelectrodes. Figure 3b illustrates recorded wideband, low-pass filtered, and high-pass filtered waveforms with the non-shielded optrode during pulsed illumination. The non-shielded optrode recorded a slow and mild peak within a low-frequency band and two fast and sharp opposite peaks corresponding to light-on and -off times within a high-frequency band. During the process, the non-shielded optrode also recorded a baseline noise of a large magnitude (~80 μVpp). Statistical results indicated a low-pass filtered averaged peak value of ~94 μV and a high-pass filtered peak-to-peak averaged value of ~519 μVpp (Fig. 3c). In Fig. 3d, the backside of the shielded optrode is depicted, where the metal shielded interlayer fully shields the recording microelectrode interconnection. With the shielding layer, a significantly reduced stimulation artifact was achieved under the same pulsed illumination parameters, as shown in Fig. 3e. The shielded optrode also exhibited significantly decreased baseline noise (~20 μVpp). Statistical results from the shielded optrode showed a low-pass filtered averaged peak value of ~22 μV, ~4 times smaller than the non-shielded one, and a high-pass filtered peak-to-peak averaged value of ~46 μVpp, ~11 times smaller than the non-shielded one (Fig. 3f). The magnitude of the baseline noise was also reduced by a factor of about 3.6 on average when operating with the shielded optrode, as illustrated in Fig. 3g. Analysis of stimulation artifacts from twelve electrode channels corresponding to all illuminated μLEDs underscore the shielding layer's crucial role in suppressing artifacts across all electrode channels (Fig. 3h), and across all tested μLED drive current from 1 to 0.4 mA (Fig. 3i). Besides, we also compared the influences of the working environment on the electrical recording ability using shielded optrodes in PBS-based agarose gel (0.6%) (Supplementary Fig. 18). These were not greatly different in electrode impedance (average ~80 kΩ), noise (average ~20 μVpp), and stimulation artifacts (average ~40 μVpp) within the low- and high-frequency bands for the PBS or PBS-based agarose gel. It implies that the device by design has robust commonality in similar brain tissue environments. Therefore, the inter-layer shielding among these different functional chiplets from CHIP process establishes a low-noise, artifact-free flexible bio-integrated electronic-photonic design, and implementation.

Studies on the origin of the optoelectronic artifacts

To better understand the origins of optoelectronic artifacts in polymer-based devices as well as propose useful guidance for the design of all future flexible bio-integrated electronic-photonic systems, we conducted individually addressed μLED control for a detailed analysis of frequency-dependent artifacts, as illustrated in Fig. 4. In the non-shielded optrode, we observed a strong correlation between the locations of μLED and electrode site regarding the magnitude of artifact within a low-frequency band (Fig. 4a, b). Sequential illumination of an independent μLED site from #1 to #6 showed consistent changes in the magnitude of artifact recorded by neighboring electrode sites from #1 to #12 (Supplementary Fig. 19). These results imply that the artifact within the low-frequency band (1–300 Hz) is most likely attributed to the optical-related effect since each μLED primarily illuminates its neighboring electrode sites (Supplementary Fig. 20). The recorded waveforms are also consistent with the result of the light-induced artifacts from previous reports[57,58]. This postulation was further confirmed by the observation that when the LED common p-interconnect wire was disconnected, the optical-related waveform disappeared (Fig. 4b, right side). On the other hand, with the same sequential illumination of the independent μLED from #1 to #6, the artifacts within a high-frequency band
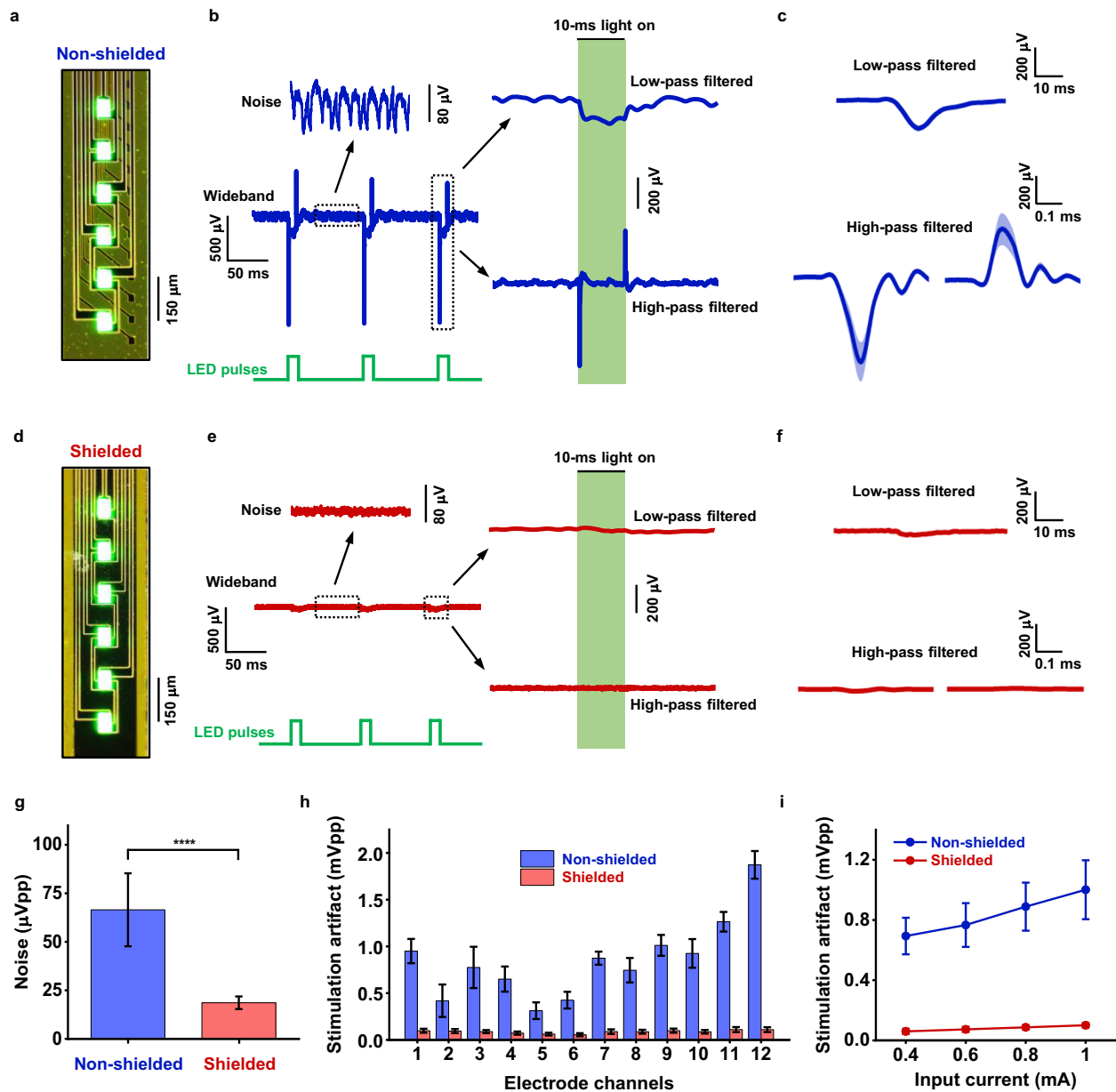
Fig. 3 | Characterization of the optoelectronic artifact of the 3D-integrated flexible optrode from CHIP. a Image of the non-shielded optrode with illumination of all μLEDs from the back side. **b** The waveforms of the recorded artifact on non-shielded optrode in the wideband and from low-pass and high-pass filtering. The data was analyzed from one representative electrode channel. **c** Averages of the low-pass and high-pass filtered waveforms based on the non-shielded optrode. **d** Image of the shielded optrode with illumination of all μLEDs from the back side. **e** The waveforms of the recorded artifact on shielded optrode in the wideband and from low-pass and high-pass filtering. The data is recorded from the same electrode location used in (**b**). **f** Averages of the low-pass and high-pass filtered waveforms from the channel based on the shielded optrode. **g** Statistical results of the recorded raw peak-to-peak magnitude of the noise for both the non-shielded and shielded optrodes. ****$P < 0.0001$. **h** Statistics of the recorded raw peak-to-peak magnitude of the stimulation artifact from twelve channels for both the non-shielded and shielded optrodes. All the μLEDs are turned on (pulse duration 10 ms, frequency 10 Hz, input current 1 mA for each μLED). **i** Statistics of the recorded raw peak-to-peak magnitude of the stimulation artifact from twelve channels with different input currents for both the non-shielded and shielded optrodes, where all the μLEDs are turned on (pulse duration 10 ms, frequency 10 Hz). All data are presented as mean ± standard deviation of the mean (s.d.m.) ($n = 5$).

(300–6000 Hz) depicted a complicated magnitude mapping, as shown in Fig. 4c. This magnitude distribution within the high-frequency band suggests an electrical-induced coupling underlying the artifacts instead of optical. To uncover the origin of this interference, we disconnected the μLED common p-interconnect wire and maintained the connection of the LED n-interconnect wires. Notably, even with no current flowing through each μLED, the electrode channels still could record sharp and fast waveforms of the same amplitude as the connected case within the high-frequency band (Fig. 4c, right side). We found that the recorded waveform only showed a single negative peak that responded to the voltage-on time. This phenomenon suggests that the artifact within the high-frequency band was mainly from the capacitive-induced coupling associated with the electrostatic effect (Supplementary Fig. 21) but not EMI. This finding is consistent with previous understanding that EMI-induced artifacts are much slower[28,53], while capacitive coupling is much faster[59]. Besides, the recorded signal with the same amplitude, depending on input voltage regardless of whether there is current flowing through, suggests that the signal is being induced by an electric field rather than a magnetic field, which
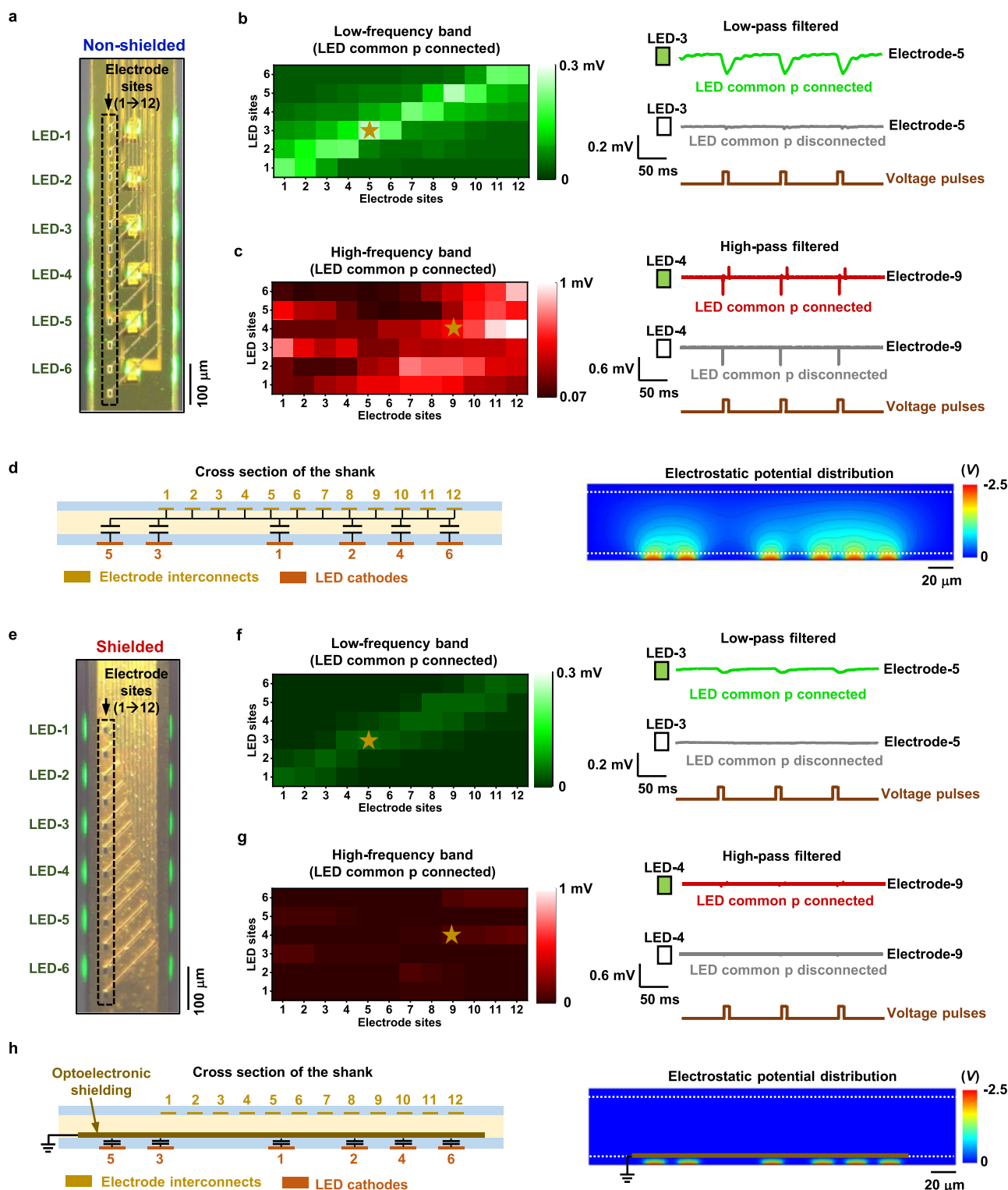
Fig. 4 | Frequency-dependent optoelectronic artifact of the 3D-integrated flexible optrode from CHIP. a The illustration of the μLED and electrode sites for the non-shielded optrode. The heat maps of the average recorded magnitude of stimulation artifact within the low-frequency band in (**b**) and within the high-frequency band in (**c**), with active single μLED from site 1 to site 6, based on the non-shielded optrode. The right side is the waveform comparison from the same channel (the graphic mark "star" from the left-side heat map) with and without μLED common p-connection from the low- and high-frequency bands, respectively. **d** Schematic illustration of the location of the μLED and electrode lines on the cross-section of the non-shielded polymer shank (twelve gold blocks: electrode recording interconnects, six orange blocks: μLED n-type driving interconnects, six equivalent plate capacitors between the μLED and electrode lines). The right side is a simulation of the electrostatic potential distribution from these μLED driving lines. **e** The illustration of the μLED and electrode sites for the shielded optrode. The heat maps of the average recorded magnitude of stimulation artifact within the low-frequency band in (**f**) and from the high-frequency band in (**g**), with active single μLED from site 1 to site 6, based on the shielded optrode. The right side is the waveform comparison from the same channel (the graphic mark "star" from the left-side heat map) with and without μLED common p-connection from the low- and high-frequency bands, respectively. **h** Schematic illustration of the location of the μLED and electrode interconnect on the cross-section of the shielded polymer shank (twelve gold blocks: electrode recording interconnects, six orange blocks: μLED n-type driving interconnects, a dark yellow block: optoelectronic shielding layer, six equivalent plate capacitors between the μLED driving lines and shielding layer). The right side is a simulation of the electrostatic potential distribution from these μLED driving lines when there is a shielding layer.

is characteristic of capacitive coupling[60]. The schematic illustration and simulation of the cross-section shank with different layered µLED and electrode wires in Fig. 4d further agreed well with the magnitude mapping of the artifacts in Fig. 4c. As depicted in Fig. 4d, the electrical field resulted from the fast-charging signals carrying on the bottom LED wires had propagated through the polymeric layers towards the top nearby electrode wires due to the electrostatic effects.

These hypotheses were further vindicated by the shielded optrode, where the microelectrodes were fully blocked from the µLED array's direct optical radiation (Fig. 4e). We observed effectively suppressed artifacts in both the low- and high-frequency bands but with highly similar spatial patterns to the non-shielded case, where there is still the linear relationship for the low-frequency case while the similar enhanced magnitude patterns among others for the high frequency (Fig. 4f, g). We attribute the remaining low-frequency band artifacts to light scattering around the environment (Supplementary Fig. 22). For high-frequency band artifacts, we observed a similar single negative peak of the same magnitude when the µLED common p interconnect was disconnected, consistent with an electrostatic origin. The remaining electrostatic effect might be through the conductive medium surrounding the devices since the grounded shielding significantly mitigated the impact of the intra-device interference by more than two orders of magnitude from simulation (Fig. 4h and Supplementary Fig. 23).

Discussion

Our findings demonstrate the significant potential of the CHIP process for creating advanced flexible electronic-photonic integrated devices. The CHIP-led prototype optrode successfully integrates multiple functionalities unprecedentedly, with also double-sided area utilization, I/O integration, and excellent miniaturization, showcasing the scalability of this approach. Notably, the CHIP process offers distinct advantages compared to conventional sequential fabrication methods or existing micro-scale stacking, especially considering functional integration, device miniaturization, and manufacturing complexity, which are further translatable to WHIP. The RT bonding further eliminates concerns about material degradation and allows for broader material compatibility. Additionally, the monolithic I/Os simplifies device connection and reduces its dimension. The robust reliability of ultrathin 3D-integrated polymer devices achieved through CHIP makes them suitable for long-term interfacing with excellent deformability. This capability will pave the way for the development of a new generation of wearable electronics, implantable medical devices, and conformable displays with integrated functionalities.

While the current prototype optrode demonstrates significant progress, future work will focus on application-specific engineering of such unprecedented device capabilities. One such application is for optotagging of neurons in the brain[61,62], where we control the activity of optogenetically-tagged neurons in a bio-safe manner and study how they influence behavior to allow for a more precise understanding of how brain circuits function. Through colocalized different color LEDs[8,15] or temporal multiplexing of the light pulses at distinct time intervals[63], it is possible to address co-expressed opsins with overlapping action wavelengths in future optotagging experiments. We envision further integration will incorporate exciting possibilities in multimodal bio-interfacing across various parameters such as electrical activity[21], chemical signaling[16,27], temperature[64,65], pressure[31,66], and even optical signatures[67]. Such comprehensive data acquisition could revolutionize our understanding of biological processes at a deeper level. The envisioned future scaling suggests the potential for chronic, cell-type-specific neural stimulation and recording[68,69]. This advancement will significantly impact several fields, including brain-computer interfaces and deep brain stimulation therapies.

Methods

Device fabrication

Fabrication of the µLED array chiplet with shielding. A transparent colorless polyimide thin film (Wuxi Shunxun New Material, 1-mil thickness) was laminated on the PDMS-coated (PDMS = 10:1, 3000 rpm) glass substrate. The µLED chip array was monolithically picked up from an µLED wafer (Sanan Optoelectronics, $34 \times 58 \times 7\,\mu m^3$ µLED chip located on the 4-inch wafer) by using a PDMS stamp. This released freestanding µLED array was printed onto the above layer with a 1.2-µm-thick SU8 (Kayaku, SU-8 2, 4000 rpm) as an adhesion. The µLED array was planarized by a 5-µm-thick SU8 (Kayaku, SU-8 2005, 3000 rpm). The photolithographic pattern and wet etching method were employed for the µLED interconnection after the sputtered metallization (Cr/Au: 10/200 nm). After the surface was insulated with a 5-µm-thick SU-8 (Kayaku, SU-8 2005, 3000 rpm), a lift-off method (MicroChemicals, AZ nLOF 2035, 3000 rpm) was processed for the shielding pattern (Cr/Au: 5/100 nm) on the top of the insulated layer.

Preparation of the PDMS stamp. A SU8 mold with dimples (Kayaku, SU-8 2075, 3000 rpm) was made upon a Si wafer. Bubble-free PDMS gel (12:1) was gently poured into this SU8 mold. The PDMS in the mold was cured at RT for two days to form a suitable sticky force and then taken out as a PDMS stamp.

Fabrication of the temperature sensor chiplet. The Kapton thin film (Fralock, half-mil thickness) was laminated on the PDMS-coated (PDMS = 10:1, 3000 rpm) glass substrate. The lift-off method (MicroChemicals, AZ nLOF 2035, 3000 rpm) and metallization were conducted for both the serpentine temperature microsensor (Cr/Pt: 5/20 nm) and interconnection (Cr/Au: 5/100 nm). Finally, the surface was insulated with a 2-µm-thick SU8 (Kayaku, SU-8 2, 3000 rpm).

Fabrication of the microelectrode array chiplet. The Kapton thin film (Fralock, half-mil thickness) was laminated on the PDMS-coated (PDMS = 10:1, 3000 rpm) glass substrate. The microelectrode array was patterned by photolithography (MicroChemicals, S1805 G2, 4000 rpm) and wet etching method after metallization (Cr/Au: 5/100 nm). Finally, the surface was encapsulated with a 5-µm-thick SU8 (Kayaku, SU-8 2005, 3000 rpm).

Electrochemical deposition of PEDOT:PSS. DI water (100 ml) was mixed with EDOT monomer (0.1% (w/v) 0.01 M, Sigma Aldrich) and NaPSS (0.7% (w/v), Sigma Aldrich) to form precursors. Silver paste (Ted Pella) was pasted gently on the pad area and dried. The copper tape was taped on the edge to have good contact with the potentiostat. Before dipping the device into the solution, gentle O_2 plasma (100 W, 1 min) was applied to the device to have good wettability with water. The 3-electrode system was applied to the device using potentiostat (reference 620, Gamry). Pt wire (0.5 mm diameter, Sigma Aldrich) was applied as the counter electrode. Ag/AgCl reference electrode was clipped in the middle of the working and counter electrodes. Potentiostatic function was used for electroplating PEDOT:PSS with a certain amount of time.

Multi-chiplet bonding and shaping. After the chiplets were checked, these ready chiplets were peeled off from their temporary substrates respectively. The biocompatible epoxy resin (Gorilla) was blended to a certain proportion by adding acetone (e.g., 1:6) and then spin-coated (4000 rpm) on the pre-bonded backside of the chiplets. Subsequently, the chiplets were aligned and bonded upon the targeted surface through alignment marks by design under a microscope. After overnight curing at RT, the monolithic chiplets were milled by UV laser (LPKF ProtoLaser U4) to form the desired shape.

Device characterization

SEM images were captured for the surface and cross-sectional morphology (Helios 5 CX DualBeam, Thermo Fisher Scientific). Optical microscopy (VHX-7000N, Keyence) was used to take sample images. µLED emission spectra were collected with a spectrometer (HR2000, Ocean Optics). Far-field angular emission profiles of the optrode were captured by a standard Si photodetector with a high-precision rotation stage (Thorlabs). Calibration and monitoring of the temperature microsensor was processed by a probe

station with a heating system (Everbeing Int'l Corp.), a semiconductor parameter analyzer (B1500A, Keysight), and a source meter (Keithley 2400). The Intan RHD recording system and amplifier (Intan Technologies) were used to measure the impedances (both the magnitude and the phase at 1 kHz) and stimulation artifacts (1–300 Hz and 300–6000 Hz bandpass filtering for the low-pass and high-pass filtered signals, respectively) in 1× phosphate-buffered saline (PBS) solution, recorded at a 20 kHz sampling rate. Pt wire (0.5 mm diameter, Sigma Aldrich) soaking in the solution was applied as the grounded electrode connected to the ground of the Intan amplifier, keeping the original zero-ohm resistor shorting the reference to the ground in the Intan headstage.

Soaking test
The shanks of the optrodes were soaked in 1× phosphate-buffered saline solution. After positioning, the beaker containing PBS was sealed. Then, the beaker was put in the oven and kept at 47 °C. When coming to be measured, the samples were taken out from the beaker and rinsed with DI water and IPA. After they were naturally dried, the samples were then gently reassembled with a PCB board, and each function was measured later. After finishing the measurement, the samples were detached from the PCB board and then fixed to the beaker for soaking.

T-peeling test
The samples were made from two pieces of Kapton (Fralock, half-mil thickness) with different thick adhesives. Adding acetone with epoxy resin (15:1, 10:1, 6:1, 1:3 volume ratio) under a rotating speed (4000 rpm) could obtain about 1, 2, 5, and 10 μm thick adhesive, respectively. Each sample (20 mm width and 40 mm length) with a 30-mm clamp base anchored in MARK-10 was used for the T-peeling test. The fixed peeling speed of 10.1 mm/min was set up.

Cyclic bending test
To perform the cyclic bending test, the devices were attached and bent through a travel stage (LTS150 Thorlabs which provides repetitive back-and-forth motion). At the end of the stage where the backward movement was completed, a blunt tip (1 mm thick glass slice) was fixed to deform the devices. The displacement of the stage was adjusted to be 1.1 mm with a speed of 1 mm/s. The probe was fixed vertically to the stage and formed with a 27° angle measured by software during the bending. The 10-, 100-, and 1000-time cyclic bendings were performed before the characterization.

Insertion test in brain phantom
The transparent hydrogel brain phantom (0.6% w/w agarose) was used to characterize the insertion dynamics. The gel solution (0.24 g of agarose in 40 g of deionized water) was prepared and heated at 140 °C for 1 h. The gel was solidified in the mold at RT for 2 h before the test. The insertion was done by Neural Glider with a constant insertion speed of 50 μm/s and perpendicular displacement of 1.5 mm.

Estimation of critical buckling force of device with different thickness
To avoid buckling before penetration, the insertion force should be less than the critical buckling force, which can be estimated by the Euler's formula[70]:

$$F_{buckling} = \frac{\pi^2 I_x E}{(KL)^2}, \ I_x = \frac{wt^3}{12}$$

Where E is Young's modulus, K is the column effective length factor, I is the area moment of inertia, and L, w, and t are the length, width, and thickness of the shank, respectively. The shanks are considered as the beam fixed at one side ($K = 0.7$) with a constant cross-sectional area. Assuming E for Kapton is 2.5 GPa, $w = 220$ μm. Here, the general puncture force estimated as 80 mN and 9 mN for rat implantation with and with dura removal was demonstrated[34]. The current design with a shank thickness of 75 um and length of 2 mm can achieve aid-free insertion with dura.

FEA

Optrode bending. The 3D finite element model was established in ABAQUS to simulate the bending of the device. To simplify the model, the metal layer and μLED components are not included but are assumed to be compliant with the thick polymeric substrate (Kapton, deformable, C3D8R). In the simulation, the three main layers with different thicknesses were considered, namely, the μLED layer (40 μm), the temperature sensor layer (20 μm), and the electrodes layer (20 μm), and the tie constrain was applied between the interface after sandwiched them to mimic the secured bonding between them. The material properties (Elastic modulus and Poisson's ratio) used in the simulations are: $E_{PDMS} = 2.5$ GPa, $v = 0.34$.

Electronic packaging. The contact analysis was demonstrated using ABAQUS. The four representative layers consisted of an acrylic top plate with four holes at the corner (deformable, C3D8R), a device pad array matrix with a cushion layer (deformable, C3D8R), and a solder ball matrix integrated PCB layer (rigid). The material properties (Elastic modulus and Poisson's ratio) used in the simulations are $E_{Acrylic} = 3.3$ GPa, $v = 0.37$; $E_{cushion} = 1.32$ MPa, $v = 0.45$.

Electrostatic analysis for the shielding effect
A 2D electrostatics model was established in COMSOL Multiphysics to investigate shielding effects between the LED and electrode layers. The LED wires were set as the anode (-2.5 V) where the device boundaries were grounded. For the situation where there was a shielding layer, extra ground was assigned to the shielding layer. Accordingly, the electrical field distribution was revealed for comparison. The electrical relative permittivity used in the simulation for gold, polyimide, and μLED were set as 6.9, 3.4, and 8.9, respectively.

μLED-drive system
This individually addressable μLED array was controlled by these electrical boards (LED171596AEVM and EK-TM4C123GXL, Texas Instruments), operated with the Energia software system. Six of the ninety-six channels were used, and the step-size setup of the accurate output current was 20 μA for each μLED. Pulse width modulation frequency was selected with 20 kHz while the rise and fall times of 50–200 ns were enabled.

PCB-connector design for one-step, low-profile connection
A four-layer board design has been employed to minimize capacitive coupling and mitigate potential crosstalk at the PCB level. The uppermost layer is exclusively dedicated to electrical recording signals, followed by a comprehensive ground layer covering the entirety of the area, except for vias. Subsequently, the layer beneath accommodates the temperature sensor, a noteworthy aspect being its complete grounding, leaving room only for the essential two wires. The bottom layer is designated explicitly for μLED control, mirroring the comprehensive grounding approach and allowing only the required interconnects. This design is geared towards effectively reducing capacitive coupling by deliberately minimizing overlapping areas in the z dimension. The customized PCB connector enables a one-step, low-profile connection with the flexible 3D-integrated optrode through a unique sandwiched structure. Conduction is meticulously established through the contact between the solder ball array on the PCB and the pad area of the probe, thus facilitating a robust connection between the rigid balls and the soft gold pad array. Functioning as a conduit, the PCB connector is pivotal in bridging the multiple data acquisition/control electronics and the integrated device, enabling seamless connectivity within the overall system.

Data availability
All data generated or analyzed during this study are included in this published article and supplementary information files.

Code availability

The underlying code for this study is not publicly available but may be made available to qualified researchers on reasonable request from the corresponding author.

References

1. Wei, Z. X. et al. Evolution of optical wireless communication for B5G/6G. *Prog. Quant. Electron.* **83**, 100398 (2022).
2. Minotto, A. et al. Visible light communication with efficient far-red/near-infrared polymer light-emitting diodes. *Light Sci. Appl.* **9**, 70 (2020).
3. Fedyanin, D. Y. & Stebunov, Y. V. All-nanophotonic NEMS biosensor on a chip. *Sci. Rep.* **5**, 10968 (2015).
4. Altug, H., Oh, S. H., Maier, S. A. & Homola, J. Advances and applications of nanophotonic biosensors. *Nat. Nanotechnol.* **17**, 5–16 (2022).
5. Taal, A. J. et al. Optogenetic stimulation probes with single-neuron resolution based on organic LEDs monolithically integrated on CMOS. *Nat. Electron.* **6**, 669–679 (2023).
6. Kim, K. et al. Artifact-free and high-temporal-resolution in vivo opto-electrophysiology with microLED optoelectrodes. *Nat. Commun.* **11**, 2063 (2020).
7. Kim, T. I. et al. Injectable, cellular-scale optoelectronics with applications for wireless optogenetics. *Science* **340**, 211–216 (2013).
8. Li, L. Z. et al. Colocalized, bidirectional optogenetic modulations in freely behaving mice with a wireless dual-color optoelectronic probe. *Nat. Commun.* **13**, 839 (2022).
9. Lee, Y. et al. Standalone real-time health monitoring patch based on a stretchable organic optoelectronic system. *Sci. Adv.* **7**, eabg9180 (2021).
10. Castaneda, D., Esparza, A., Ghamari, M., Soltanpur, C. & Nazeran, H. A review on wearable photoplethysmography sensors and their potential future applications in health care. *Int. J. Biosens. Bioelectron.* **4**, 195–202 (2018).
11. Kim, T. H. et al. Fully stretchable optoelectronic sensors based on colloidal quantum dots for sensing photoplethysmographic signals. *Acs. Nano.* **11**, 5992–6003 (2017).
12. Lee, I., Probst, D., Klonoff, D. & Sode, K. Continuous glucose monitoring systems-current status and future perspectives of the flagship technologies in biosensor research. *Biosens. Bioelectron.* **181**, 113054 (2021).
13. Alsunaidi, B., Althobaiti, M., Tamal, M., Albaker, W. & Al-Naib, I. A review of non-invasive optical systems for continuous blood glucose monitoring. *Sensors* **21**, 6820 (2021).
14. Cai, X. et al. A wireless optoelectronic probe to monitor oxygenation in deep brain tissue. *Nat. Photon.* 1–9 (2024).
15. Cai, X. et al. A dual-channel optogenetic stimulator selectively modulates distinct defensive behaviors. *Iscience* **25**, 103681 (2022).
16. Liu, C. B. et al. A wireless, implantable optoelectrochemical probe for optogenetic stimulation and dopamine detection. *Microsyst. Nanoeng.* **6**, 64 (2020).
17. Song, H. L. et al. Highly-integrated, miniaturized, stretchable electronic systems based on stacked multilayer network materials. *Sci. Adv.* **8**, eabm3785 (2022).
18. Biswas, S. et al. Integrated multilayer stretchable printed circuit boards paving the way for deformable active matrix. *Nat. Commun.* **10**, 4909 (2019).
19. Huang, Z. L. et al. Three-dimensional integrated stretchable electronics. *Nat. Electron.* **1**, 473–480 (2018).
20. Li, L. Z. et al. Transfer-printed, tandem microscale light-emitting diodes for full-color displays. *Proc. Natl Acad. Sci. USA* **118**, e2023436118 (2021).
21. Obaid, S. N. et al. Design and fabrication of a flexible opto-electric biointerface for multimodal optical fluorescence and electrical recording. *Acs. Appl. Electron. Mater.* **5**, 1688–1696 (2023).
22. Mao, D. C., Sun, F., Driscoll, B., Li, Z. H. & Xu, G. Y. Close-packed dual-color micro-LEDs enable cortical-layer-specific bidirectional optogenetic electrophysiology. *Cell Rep. Phys. Sci.* **4**, 101702 (2023).
23. Reddy, J. W. et al. High density, double-sided, flexible optoelectronic neural probes with embedded muLEDs. *Front. Neurosci.* **13**, 745 (2019).
24. Chen F. R. et al. Mass transfer techniques for large-scale and high-density microLED arrays. *Int. J. Extreme. Manuf.* **4**, 042005 (2022)
25. Ko, E., Vöröslakos, M., Buzsáki, G. & Yoon, E. FlexLiTE: flexible micro-LED integrated optoelectrodes for minimally-invasive chronic deep-brain study. *bioRxiv* (2022).
26. Ji, B. et al. Flexible polyimide-based hybrid opto-electric neural interface with 16 channels of micro-LEDs and electrodes. *Microsyst. Nanoeng.* **4**, 27 (2018).
27. Ling, W. et al. Flexible electronics and materials for synchronized stimulation and monitoring in multi-encephalic regions. *Adv. Funct. Mater.* **30**, 2002644 (2020).
28. Guo, Z. J. et al. A polyimide-based flexible optoelectrodes for low-noise neural recording. *IEEE Electr. Device Lett.* **40**, 1190–1193 (2019).
29. Yan, D. et al. Self-assembled origami neural probes for scalable, multifunctional, three-dimensional neural interface. *bioRxiv*. (2024).
30. Jang, J. et al. 3D heterogeneous device arrays for multiplexed sensing platforms using transfer of perovskites. *Adv. Mater.* **33**, e2101093 (2021).
31. Han, M. et al. Catheter-integrated soft multilayer electronic arrays for multiplexed sensing and actuation during cardiac surgery. *Nat. Biomed. Eng.* **4**, 997–1009 (2020).
32. Kuliasha, C. A. & Judy, J.W. The materials science foundation supporting the microfabrication of reliable polyimide-metal neuroelectronic interfaces. *Adv. Mater. Technol.* **6**, 2100149 (2021).
33. Vinnikova, S., Fang, H. & Wang, S.D. Mechanics of regular-shape nanomeshes for transparent and stretchable devices. *J. Appl. Mech.* **87**, 101010 (2020).
34. Chen, L. et al. Flexible high-resolution force and dimpling measurement system for pia and dura penetration during microelectrode insertion into rat brain. *IEEE Trans. Biomed. Eng.* **68**, 2602–2612 (2021).
35. Cok, R. S. et al. Inorganic light-emitting diode displays using micro-transfer printing. *J. Soc. Inform. Disp.* **25**, 589–609 (2017).
36. Neto, J. P. et al. Does impedance matter when recording spikes with polytrodes? *Front. Neurosci.* **12**, 715 (2018).
37. Ludwig, K. A., Uram, J. D., Yang, J. Y., Martin, D. C. & DR, Kipke Chronic neural recordings using silicon microelectrode arrays electrochemically deposited with a poly(3,4-ethylenedioxythiophene) (PEDOT) film. *J. Neural Eng.* **3**, 59–70 (2006).
38. Vitoratos, E. et al. Thermal degradation mechanisms of PEDOT:PSS. *Org. Electron.* **10**, 61–66 (2009).
39. Friedel, B. et al. Effects of layer thickness and annealing of PEDOT:PSS layers in organic photodetectors. *Macromolecules* **42**, 6741–6747 (2009).
40. Shin, Y. et al. Array-wide uniform PEDOT:PSS electroplating from potentiostatic deposition. *Biosens. Bioelectron.* **261**, 116418 (2024).
41. Terakita, A. The opsins. *Genome Biol.* **6**, 213 (2005).
42. Mei, Y. et al. Improvement of the emission intensity of gan-based micro-light emitting diodes by a suspended structure. *Acs Photon.* **9**, 3967–3973 (2022).
43. Stark, E., Koos, T. & Buzsaki, G. Diode probes for spatiotemporal optical control of multiple neurons in freely moving animals. *J. Neurophysiol.* **108**, 349–363 (2012).
44. Scharf, R. et al. Depth-specific optogenetic control in vivo with a scalable, high-density muLED neural probe. *Sci. Rep.* **6**, 28381 (2016).

45. Khurram, A. & Seymour, J. P. Investigation of the photoelectrochemical effect in optoelectrodes and potential uses for implantable electrode characterization. *Annu. Int. Conf. IEEE Eng. Med. Biol. Soc.* **2013**, 3032–3035 (2013).

46. Shin, H. et al. Multifunctional multi-shank neural probe for investigating and modulating long-range neural circuits in vivo. *Nat. Commun.* **10**, 3777 (2019).

47. Yona, G., Meitav, N., Kahn, I. & Shoham, S. Realistic numerical and analytical modeling of light scattering in brain tissue for optogenetic applications(1,2,3). *eneuro* **3**, 1–9 (2016).

48. Owen, S. F., Liu, M. H. & Kreitzer, A. C. Thermal constraints on in vivo optogenetic manipulations. *Nat. Neurosci.* **22**, 1061–1065 (2019).

49. Yizhar, O., Fenno, L. E., Davidson, T. J., Mogri, M. & Deisseroth, K. Optogenetics in neural systems. *Neuron* **71**, 9–34 (2011).

50. Ferenczi, E. A., Tan, X. Q. & Huang, C. L. H. Principles of optogenetic methods and their application to cardiac experimental systems. *Front/ Physiol.* **10**, 1096 (2019).

51. Forli, A., Pisoni, M., Printz, Y., Yizhar, O. & Fellin, T. Optogenetic strategies for high-efficiency all-optical interrogation using blue-light-sensitive opsins. *Elife* **10**, e63359 (2021).

52. Jun, J. J. et al. Fully integrated silicon probes for high-density recording of neural activity. *Nature* **551**, 232–236 (2017).

53. Kampasi, K. et al. Dual color optogenetic control of neural populations using low-noise, multishank optoelectrodes. *Microsyst. Nanoeng.* **4**, 10 (2018).

54. Qiang, Y. et al. Crosstalk in polymer microelectrode arrays. *Nano. Res.* **14**, 3240–3247 (2021).

55. Guo, B. et al. Flexible neural probes with electrochemical modified microelectrodes for artifact-free optogenetic applications. *Int. J. Mol. Sci.* **22**, 11528 (2021).

56. Ji, B. et al. Flexible and stretchable opto-electric neural interface for low-noise electrocorticogram recordings and neuromodulation in vivo. *Biosens. Bioelectron.* **153**, 112009 (2020).

57. Cho, Y. U. et al. Ultra-low cost, facile fabrication of transparent neural electrode array for electrocorticography with photoelectric artifact-free optogenetics. *Adv. Funct. Mater.* **32**, 2105568 (2022).

58. Liu, X., Lu, Y., Iseri, E., Shi, Y. & Kuzum, D. A compact closed-loop optogenetics system based on artifact-free transparent graphene electrodes. *Front. Neurosci.* **12**, 132 (2018).

59. Heydari, P. & Pedram, M. Capacitive coupling noise in high-speed VLSI circuits. *IEEE Trans. Comput. Aid Des. Integr. Circ. Syst.* **24**, 478–488 (2005).

60. Qiu, L., Yuan, S. F., Shi, X. L. & Huang, T. X. Design of piezoelectric transducer layer with electromagnetic shielding and high connection reliability. *Smart Mater. Struct.* **21,** 075032 (2012).

61. Rost, B. R., Wietek, J., Yizhar, O. & Schmitz, D. Optogenetics at the presynapse. *Nat. Neurosci.* **25**, 984–998 (2022).

62. Emiliani, V. et al. Optogenetics for light control of biological systems. *Nat. Rev. Method Prime* **2**, 55 (2022).

63. Dwijayanti, A., Zhang, C., Poh, C. L. & Lautier, T. Toward multiplexed optogenetic circuits. *Front. Bioeng. Biotechnol.* **9**, 804563 (2021).

64. Reeder, J. T. et al. Soft, bioresorbable coolers for reversible conduction block of peripheral nerves. *Science* **377**, 109 (2022).

65. Zhao, X. F. et al. A fully flexible intelligent thermal touch panel based on intrinsically plastic ags semiconductor. *Adv. Mater.* **34**, e2107479 (2022).

66. Nie, Z. Y., Kwak, J. W., Han, M. D. & Rogers, J. A. Mechanically active materials and devices for bio-interfaced pressure Sensors-A review. *Adv. Mater.* https://doi.org/10.1002/adma.202205609 (2023).

67. Mehidine, H. et al. Optical signatures derived from deep UV to NIR excitation discriminates healthy samples from low and high grades glioma. *Sci. Rep.* **9**, 8786 (2019).

68. John, J., Li, Y. F., Zhang, J. S., Loeb, J. A. & Xu, Y. Microfabrication of 3D neural probes with combined electrical and chemical interfaces. *J. Micromech. Microeng.* **21**, 105011 (2011).

69. Du, J. G., Roukes, M. L. & Masmanidis, S.C. Dual-side and three-dimensional microelectrode arrays fabricated from ultra-thin silicon substrates. *J. Micromech. Microeng.* **19**, 075008 (2009).

70. Geramifard, N. et al. Insertion mechanics of amorphous SiC ultra-micro scale neural probes. *J. Neural Eng.* **19**, 026033 (2022).

Author contributions
Y.H. and H.F. developed the concepts, designed the devices, and performed artifact analysis. Y.H. and Y.S. performed fabrication and characterization. G.L. performed numerical simulations and mechanical characterization. T.B. designed and assembled the PCB board. Y.H. and X.W. performed optical characterization. A.M., P.B., and C.C. developed the optrode concept and design. J.L. and H.F. provided tools and supervised the research. Y.H. and H.F. wrote the paper in consultation with the rest of the authors.

Competing interests
The authors declare no competing interests.

Additional information
Supplementary information The online version contains supplementary material available at https://doi.org/10.1038/s41528-024-00344-w.

Correspondence and requests for materials should be addressed to Hui Fang.

Reprints and permissions information is available at http://www.nature.com/reprints

Publisher's note Springer Nature remains neutral with regard to jurisdictional claims in published maps and institutional affiliations.